A new open boundary formulation for incompressible SPH

Agnès Leroy, Damien Violeau, Martin Ferrand, Louise Fratter, Antoine Joly

A new open boundary formulation for incompressible SPH

A. Leroy[a,b,*], D. Violeau[a,b], M. Ferrand[a], L. Fratter[a], A. Joly[a,b]

[a] *EDF R&D, Chatou, France*
[b] *LHSV, Ecole des Ponts, CEREMA, EDF R&D, UPE, Chatou, France*

Abstract

In this work a new formulation for inflow/outflow boundary conditions in an incompressible Smoothed Particles Hydrodynamics (ISPH) model is proposed. It relies on the technique of unified semi-analytical boundary conditions that was first proposed for wall boundary conditions in 2013, then extended to open boundaries in the framework of weakly-compressible SPH (WCSPH). An ISPH model relying on that formulation for solid boundaries was then proposed, which is the one considered here. It includes a buoyancy model for temperature effects and a $k-\epsilon$ turbulence closure. There are two main requirements for the imposition of open boundaries in ISPH: an algorithm to let particles enter and leave the domain, and the correct imposition of open boundary conditions on the fields. Regarding the algorithm for particles creation/destruction, it relies on the variation of mass of the particles located at the open boundaries. When the mass of such a particle reaches a threshold, a new particle is released. On the other hand, the imposition of open boundary conditions on the fields is done by prescribing the value of the boundary terms appearing in the semi-analytical formulation. The formulation was first validated in 2-D on a cut dam-break, a case of propagation of a solitary wave and a Creager weir. It was then extended to 3-D and tested on a 3-D circular pipe. A preliminary application case consisting of two connected pipes at different temperatures was then simulated. The results are promising since in all cases the fluid enters and leaves the domain as prescribed and generating none or very few reflected waves.

Keywords: SPH, incompressible, open boundary conditions

*Corresponding author. *tel*: +33 (0)6 67 88 92 13
Email address: agnes.leroy@edf.fr (A. Leroy)

1. Introduction

The high computational cost of the Smoothed Particle Hydrodynamics (SPH) method restrains the range of application in fluid dynamics to rather short scale problems, so that an efficient formulation for open boundaries is required for its use on an industrial level. Such a formulation would make it possible to accurately represent flows in truncated domains and is a first step towards the coupling of SPH with other numerical methods. However, the prescription of boundary conditions in SPH is problematic, especially when it comes to open boundary conditions.

Regarding wall boundary conditions, several methods have been proposed until now, the most classical ones in the SPH community being *i*) the imposition of repulsive forces at the boundary [1, 2], *ii*) the use of ghost particles across the boundary [3, 4, 5] and *iii*) the use of mirror particles across the boundary [6]. Another class of methods is also starting to gain importance, where the SPH interpolation is renormalised so as to restore its consistency close to boundaries [7]. The accuracy of the renormalisation process and the treatment of the boundary terms are the two key-issues of this technique. They led to several works [7, 8, 9, 10, 11, 12, 13] which made it possible to accurately represent flows close to solid boundaries and to prescribe arbitrary Neumann or Dirichlet boundary conditions. Ferrand *et al.* [10] obtained good results with a $k-\epsilon$ turbulence model where Neumann boundary conditions could be prescribed exactly on k and ϵ for the first time in SPH, the condition on the turbulent dissipation rate ϵ being non-homogeneous.

On the other hand, three types of methods have been proposed regarding open boundary conditions. First, methods where particles are let to enter or leave the domain through the use of buffer layers (see [14] for example). The open boundary conditions are then prescribed by setting the physical quantities of the particles in the buffer zones. The second type of method relies on the semi-analytical boundary conditions [15]. The open boundaries are discretised like walls: through a mesh with particles at the vertices. The mass of these particles is let to evolve so as to inject or remove mass from the computational domain and the boundary conditions are accurately prescribed through the boundary

terms of the differential operators, which run over the boundary mesh elements (segments in 2-D, triangles in 3-D). This kind of method is more complex than the ones based on buffer layers but makes it possible to accurately prescribe open boundary conditions on the fields, as was shown in [15]. A third kind of method was recently proposed in [16], based on the mirror particles technique. In this work the mirror axis of each particle moves at the open boundary, and new particles are created behind that axis when it reaches a limit position.

Regardless of the method chosen to discretise open boundaries, with weakly compressible SPH (WCSPH) the prescription of the fields at inflow or outflow boundaries should be done based on the theory of Riemann invariants, since a hyperbolic system of equations is then solved [17, 15]. Otherwise, prescribing both the pressure and the velocity at an open boundary may result in spurious waves. This is not the case when it comes to the incompressible SPH method (ISPH), where a pressure Poisson equation is solved. ISPH was developed as an alternative to WCSPH in order to improve the pressure estimation [5, 18]. In this approach the correct prescription of boundary conditions is a key-point for the accuracy of the scheme. The first ISPH models were based on ghost or mirror particles for solid walls, which do not make it possible to accurately prescribe arbitrary boundary conditions on the pressure. With the projection method employed in these models, a non-homogeneous boundary condition should be applied on the pressure, which was made possible with the work by Leroy *et al.* [12]. Indeed, they proposed an ISPH model based on the semi-analytical boundaries, with correct pressure wall boundary conditions. The accuracy of the model was shown to reach that of mesh-based methods, especially on confined flows. The formulation employed for the free-surface treatment in that work remains problematic, since it involves the detection of the free-surface particles and the prescription of their pressure to zero. A new free-surface formulation was proposed in [19], that does not involve any tracking of the interface anymore, but it would have to be adapted to the USAW framework. In the present work, we thus use the same formulation for the free-surface as in [12].

ISPH is nevertheless a promising method for industrial applications, even regarding confined flows where mesh-based methods find it hard to simulate flows around moving bodies that come to touch each other for instance. In

order to apply the method to real cases, a formulation for open boundaries is necessary.

Few works regarding open boundary conditions for ISPH have been proposed until now, some based on the buffer layers technique (see [20] for example) and the one cited earlier ([16]) based on mirror particles.

The present work is thus an extension of the work proposed in [12] to the treatment of open boundaries in ISPH, based on the semi-analytical boundary conditions. The ISPH model considered here includes a $k-\epsilon$ turbulence closure (see also [21, 22]) and a buoyancy model. First, the model will be described with emphasis on the prescription of the pressure boundary condition at open boundaries. Then, the results obtained on several 2-D validation cases will be presented, before showing first results in 3-D.

2. Governing equations and modelling choices

The system of equations to be solved is composed of the incompressible Reynolds-Averaged Navier-Stokes (RANS) equations coupled to a heat equation and to the $k-\epsilon$ turbulence closure. The Boussinesq approximation is used to account for density variations so that the system reads [23]:

$$\begin{cases} \boldsymbol{\nabla} \cdot \boldsymbol{v} = 0 \\ \dfrac{dk}{dt} = \mathbb{P} + \mathbb{G} - \epsilon + \dfrac{1}{\rho}\nabla \cdot (\mu_k \boldsymbol{\nabla} k) \\ \dfrac{d\epsilon}{dt} = \dfrac{\epsilon}{k}\left(C_{\epsilon_1}\mathbb{P} + C_{\epsilon_3}\mathbb{G} - C_{\epsilon_2}\epsilon\right) + \dfrac{1}{\rho}\nabla \cdot (\mu_\epsilon \boldsymbol{\nabla} \epsilon) \\ \dfrac{d\boldsymbol{v}}{dt} = -\dfrac{1}{\rho}\boldsymbol{\nabla}\tilde{p} + \dfrac{1}{\rho}\boldsymbol{\nabla} \cdot (\mu_E \boldsymbol{\nabla} \boldsymbol{u}) + \boldsymbol{g}\left(1 - \beta(T - T_0)\right) \\ \dfrac{d\boldsymbol{r}}{dt} = \boldsymbol{v} \\ \dfrac{dT}{dt} = K_E \nabla^2 T \end{cases} \tag{1}$$

In this system, $\boldsymbol{r}$ is the particle position, $\boldsymbol{v}$ is the Lagrangian velocity and $\boldsymbol{u}$ is the Eulerian velocity. Both velocities are equal in our SPH model except for boundary particles. When the $k-\epsilon$ turbulence closure is used, the Eulerian velocity of wall boundary particles is prescribed with a wall function (see [12]). On the other hand, at open boundaries the particles' Eulerian velocity is set as the ingoing/outgoing velocity, as we will see in Section 5.2. For all open boundaries, the Lagrangian velocity is equal to zero, whereas it is possible to

represent moving solid walls [12]. t is the time, ρ is the density (which is assumed constant in the framework of the Boussinesq approximation for weakly buoyant flows), k is the turbulent kinetic energy field, ϵ is its dissipation rate, μ is the dynamic molecular viscosity (which may be a function of the temperature), μ_T is the dynamic eddy viscosity, $\mu_E = \mu + \mu_T$ is the effective (*i.e.* total) dynamic viscosity. We also define the two variables $\mu_k = \mu + \dfrac{\mu_T}{\sigma_k}$ and $\mu_\epsilon = \mu + \dfrac{\mu_T}{\sigma_\epsilon}$. σ_k, C_{ϵ_1}, C_{ϵ_2} and σ_ϵ are model constants described in Table 1. The kinematic molecular viscosity is denoted by $\nu = \frac{\mu}{\rho}$ and the eddy viscosity by $\nu_T = \frac{\mu_T}{\rho}$. ν_T is modelled as a function of k and of ϵ as usual [24]:

$$\nu_T = C_\mu \frac{k^2}{\epsilon} \tag{2}$$

where C_μ is a constant defined in Table 1. Note that the eddy viscosity is imposed equal to zero at the walls. In case of a laminar flow, ν_T is set to zero and the k and ϵ equations are not solved.

$\boldsymbol{g}$ is the gravity field (of magnitude $g = 9.81ms^{-2}$), $\tilde{p} = p + \frac{2}{3}\rho k$ with p the pressure, β is the coefficient of thermal expansion, T is the temperature field, T_0 is the mean temperature. $K_E = K + K_T$ is the effective thermal diffusivity, with K the molecular thermal diffusivity and $K_T = \frac{\nu_T}{Pr_T}$, Pr_T being the turbulent Prandtl number, taken as 0.85 (see *e.g.* [25]). $\mathbb{P}$ is the production of turbulent kinetic energy and $\mathbb{G}$ is a buoyancy production/destruction term. $C_{\epsilon 3}$ is set to 1 if $\mathbb{G} \leq 0$ and 0 otherwise. $\mathbb{P}$ is calculated according to a mixed linear-quadratic model [26]:

$$\mathbb{P} = \min\left(\sqrt{C_\mu} k S, \nu_T S^2\right) \tag{3}$$

where $S = \sqrt{2\boldsymbol{S} : \boldsymbol{S}}$ is the scalar mean rate-of-strain. $\mathbb{G}$ is a buoyancy production/destruction term modelled through [25]:

$$\mathbb{G} = \beta K_T \boldsymbol{\nabla} T \cdot \boldsymbol{g} \tag{4}$$

3. SPH interpolation in the frame of unified semi-analytical wall boundary conditions

In this section we summarise the unified semi-analytical wall (USAW) boundary conditions used herein. In this work, fluid particles which do not belong to a boundary are called free particles $a \in \mathcal{F}$. Solid and liquid boundaries are

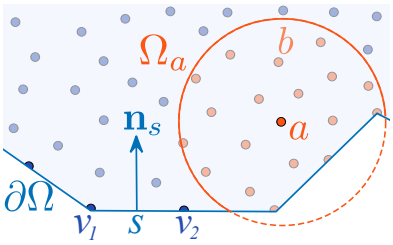

Figure 1: Sketch of the different sets of entities involved in the representation of the USAW boundary conditions.

modelled by vertex particles $v \in \mathcal{V}$ and segments $s \in \mathcal{S}$ (see Figure 1). The vertex particles are truncated fluid particles placed at the boundary that are introduced to compute more accurately the fields and their derivatives close to the walls. They are specially important when dealing with turbulence, where the fields values at the wall are required for the imposition of the boundary conditions. The segments link the vertex particles together, thus composing a mesh of the solid boundary. They are only used to compute boundary integrals, similarly to what was done by Feldman and Bonet [8]. In 2-D they are segments of length δr, whereas in 3-D they are triangles of typical size δr, with δr the initial interparticle spacing. The set of all fluid particles, including free and vertex particles, is denoted by P and particles belonging to $P = F \cup V$ are denoted by a or b. This discretisation is illustrated on Figure 1.

In this framework, the discrete SPH differential operators are different from the classical ones [10]. The antisymmetric form of the discrete SPH gradient of a field A at particle a reads:

$$(\boldsymbol{\nabla} A)_a \approx \mathbf{G}_a^{\gamma,+}\{A_b\} = \frac{1}{\gamma_a}\sum_{b\in\mathcal{P}} V_b\,(A_a + A_b)\,\boldsymbol{\nabla} w_{ab} - \frac{1}{\gamma_a}\sum_{s\in\mathcal{S}} (A_a + A_s)\,\boldsymbol{\nabla}\gamma_{as} \quad (5)$$

where V_b is the volume of particle b defined as $V_b = \frac{m_b}{\rho}$, with m_b the mass of the particles. The density being kept constant in ISPH, we will omit the particle subscript in its notation. The particles' mass is also constant, except for vertex particles located at open boundaries. On the other hand, $w_{ab} = w_h(\mathbf{r}_a - \mathbf{r}_b)$, with $\mathbf{r}$ the position and w_h the SPH kernel: in this work the $5th$ order Wendland kernel [27]. γ_a is the wall renormalisation factor mentioned in the introduction,

defined as in [7] and [10]:

$$\gamma_a = \int_{\Omega \cap \Omega_a} w(\mathbf{r}_a - \mathbf{r}') d^n \mathbf{r}' \tag{6}$$

where Ω is the fluid domain, Ω_a is the compact support of the kernel at particle a and n is the space dimension. Note that γ_a is equal to 1 far from boundaries, due to the normalisation property of the kernel. On the other hand, γ_a is inferior to 1 when the kernel support intersects the wall, as in Figure 1. γ_a is computed through the analytical formula proposed in [12] in 2-D and through a dynamic governing equation in 3-D, as in [10]. $\boldsymbol{\nabla}\gamma_{as}$ is the contribution of segment s to the gradient of γ_a, defined as:

$$\boldsymbol{\nabla}\gamma_{as} = \int_{\partial\Omega_s \cap \Omega_a} w(\mathbf{r}_a - \mathbf{r}') \mathbf{n}_s d^{n-1} \mathbf{r}' \tag{7}$$

$\partial\Omega_s$ is the boundary area spanned by segment s and $\mathbf{n}_s$ is the inward unit normal to the wall on s (see Figure 1). The following property holds [10]:

$$\boldsymbol{\nabla}\gamma_a = \sum_{s \in \mathcal{S}} \boldsymbol{\nabla}\gamma_{as} \tag{8}$$

The terms $\boldsymbol{\nabla}\gamma_{as}$ are computed through an analytical formula in 2D [10] and in 3D [13, 28].

It is also possible to define a discrete symmetric gradient:

$$(\boldsymbol{\nabla} A)_a \approx \mathbf{G}_a^{\gamma,-}\{A_b\} = -\frac{1}{\gamma_a} \sum_{b \in \mathcal{P}} V_b A_{ab} \boldsymbol{\nabla} w_{ab} + \frac{1}{\gamma_a} \sum_{s \in \mathcal{S}} A_{as} \boldsymbol{\nabla}\gamma_{as} \tag{9}$$

where $A_{ab} = A_a - A_b$ and $A_{as} = A_a - A_s$. In case the discrete gradient of a vector field is calculated, the formulae (5) and (9) remain unchanged except that $A_{ab}\boldsymbol{\nabla} w_{ab}$ and $A_{as}\boldsymbol{\nabla}\gamma_{as}$ are replaced by $\mathbf{A}_{ab} \otimes \boldsymbol{\nabla} w_{ab}$ and $\mathbf{A}_{ab} \otimes \boldsymbol{\nabla}\gamma_{as}$ respectively. In ISPH, it is important to use skew-adjoint gradient and divergence operators since the projection method is based on this property at the continuous level [29]. In this work we use an antisymmetric SPH gradient and a symmetric SPH divergence operator. Their skew-adjointness properties are reviewed in [9, 11]. The symmetric form of the SPH divergence operator reads:

$$(\nabla \cdot \mathbf{A})_a \approx D_a^{\gamma}\{\mathbf{A}_b\} = -\frac{1}{\gamma_a} \sum_{b \in \mathcal{P}} V_b \mathbf{A}_{ab} \cdot \boldsymbol{\nabla} w_{ab} + \frac{1}{\gamma_a} \sum_{s \in \mathcal{S}} \mathbf{A}_{as} \cdot \boldsymbol{\nabla}\gamma_{as} \tag{10}$$

Finally, the discrete Laplacian operator proposed by Ferrand *et al.* [10]

reads:

$$
\begin{aligned}
[\nabla\cdot(B\boldsymbol{\nabla}A)]_a \approx L_a^{\gamma}\{B_b,A_b\} \quad &= \frac{2}{\gamma_a}\sum_{b\in\mathcal{P}} V_b B_{ab}\frac{A_{ab}}{r_{ab}^2}\mathbf{r}_{ab}\cdot\boldsymbol{\nabla}w_{ab} \\
&-\frac{1}{\gamma_a}\sum_{s\in\mathcal{S}}\left[B_s\left(\boldsymbol{\nabla}A\right)_s + B_a\left(\boldsymbol{\nabla}A\right)_a\right]\cdot\boldsymbol{\nabla}\gamma_{as}
\end{aligned}
\tag{11}
$$

where B is a diffusion coefficient for the field A, B_{ab} is a mean value between a and b (here the arithmetic mean) $\mathbf{r}_{ab}=\mathbf{r}_a-\mathbf{r}_b$ and $r_{ab}=|\mathbf{r}_{ab}|$. In case $\mathbf{A}$ is a vector, the Laplacian will be denoted by $\mathbf{L}_a^{\gamma}\{B_b,\mathbf{A}_b\}$. In case $B=1$, it will be denoted by $L_a^{\gamma}\{A_b\}$. The boundary term of the Laplacian operator is simplified so that the SPH Laplacian operator used here reads:

$$
\begin{aligned}
[\nabla\cdot(B\boldsymbol{\nabla}A)]_a \approx L_a^{\gamma}\{B_b,A_b\} \quad &= \frac{1}{\gamma_a}\sum_{b\in\mathcal{P}} V_b(B_a+B_b)\frac{A_{ab}}{r_{ab}^2}\mathbf{r}_{ab}\cdot\boldsymbol{\nabla}w_{ab} \\
&-\frac{2}{\gamma_a}\sum_{s\in\mathcal{S}} B_s\left(\boldsymbol{\nabla}A\right)_s\cdot\boldsymbol{\nabla}\gamma_{as}
\end{aligned}
\tag{12}
$$

4. Incompressible SPH with the unified semi-analytical boundary conditions

In the ISPH model considered here the Chorin projection method [30] is used to solve the Navier-Stokes equations, as in [5, 12]. The space-time discretisation of system (1) thus reads, $\forall a\in\mathcal{F}$, $\forall b\in\mathcal{P}\cup\mathcal{S}$:

$$
\begin{cases}
\dfrac{k_a^{n+1}-k_a^n}{\delta t} = \mathbb{P}_a^n + \mathbb{G}_a - \epsilon_a^n\dfrac{k_a^{n+1}}{k_a^n} + \dfrac{1}{\rho}L_a^{\gamma}\left\{\mu_{k,b},k_b^n\right\} \\
\dfrac{\epsilon_a^{n+1}-\epsilon_a^n}{\delta t} = \dfrac{\epsilon_a^n}{k_a^n}\left(C_{\epsilon_1}\mathbb{P}_a^n + C_{\epsilon_3}\mathbb{G}_a - C_{\epsilon_2}\epsilon_a^{n+1}\right) + \dfrac{1}{\rho}L_a^{\gamma}\left\{\mu_{\epsilon,b},\epsilon_b^n\right\} \\
\dfrac{\tilde{\boldsymbol{v}}_a^{n+1}-\boldsymbol{v}_a^n}{\delta t} = \boldsymbol{L}_a^{\gamma}\{\nu_{T,b}^{n+1},\boldsymbol{u}_b^n\} - \left[\beta(T_a^n-T_0)-1\right]\boldsymbol{g} \\
L_a^{\gamma}\{p_b^{n+1}\} = \dfrac{\rho}{\delta t}D_a^{\gamma}\{\tilde{\boldsymbol{v}}_b^{n+1}\} \\
\dfrac{\boldsymbol{v}_a^{n+1}-\tilde{\boldsymbol{v}}_a^{n+1}}{\delta t} = -\dfrac{1}{\rho}\boldsymbol{G}_a^{\gamma,+}\{p_b^{n+1}\} \\
\dfrac{T_a^{n+1}-T_a^n}{\delta t} = L_a^{\gamma}\{K_{T,b}^{n+1},T_b^n\} \\
\boldsymbol{r}_a^{n+1} = \boldsymbol{r}_a^n + \delta t\boldsymbol{v}_a^{n+1}
\end{cases}
\tag{13}
$$

where $\tilde{\boldsymbol{v}}_a^{n+1}$ is a predicted velocity field. A particle shift is also used for stabilisation reasons. It consists in an additional particle motion based on a Fickian diffusion law, adapted to the USAW boundary conditions. For a more detailed description of this particle shift see [18, 31, 12].

The time-step size δt must satisfy several conditions to ensure the stability of the scheme (see [32]). Here an empirical criterion on the time step size is used, as in [12].

The wall boundary conditions on the pressure are obtained by projecting the third line of (13) onto the normal to the wall, and prescribing the wall boundary condition on the velocity: $\boldsymbol{v}^{n+1} \cdot \boldsymbol{n} = 0$. For all the segments s belonging to wall boundaries, this yields:

$$\left(\frac{\partial p}{\partial \boldsymbol{n}}\right)_s^{n+1} = \frac{\rho}{\delta t}\tilde{\boldsymbol{v}}_s^{n+1} \cdot \boldsymbol{n}_s = \left(\rho \boldsymbol{g} + \mu \boldsymbol{\nabla}^2 \boldsymbol{u}_s^n\right) \cdot \boldsymbol{n}_s \tag{14}$$

As in [5, 31, 12], the free-surface particles are detected through a criterion on the value of the position divergence and a zero pressure is prescribed at free-surface particles. This ISPH model with USAW boundary conditions for walls was widely verified in [12, 33].

5. Open boundaries for ISPH with the semi-analytical boundary conditions

There are two main requirements for the imposition of open boundaries in an ISPH model: an algorithm to let particles enter and leave the domain, and the correct imposition of open boundary conditions on the fields, in particular on the pressure.

5.1. Particles creation/destruction

Regarding the algorithm for particles creation/destruction, the technique proposed by Kassiotis *et al.* in [15] is used. The idea is to let the masses of the inlet/outlet vertex particles $v \in \mathcal{V}_{i/o}$ evolve over time as a function of the desired ingoing/outgoing mass flux through the inlet/outlet segments $s \in \mathcal{S}_{i/o}$ directly connected to v. The vertex particles are then used to create/delete fluid particles. The mass evolution should not introduce any perturbations in the flow, so care must be taken that its evolution is smooth. The time-derivative of the mass, denoted by $\dot{m}_v^n$, is determined by the Eulerian velocity $\boldsymbol{u}_s$ imposed at the open boundaries:

$$\forall v \in \mathcal{V}_{i/o}, \quad \dot{m}_v^n = \frac{1}{N_{sv}} \sum_{s \in \mathcal{N}_{sv}} \rho S_s (\boldsymbol{u}_s - \boldsymbol{v}_s) \cdot \boldsymbol{n}_s \tag{15}$$

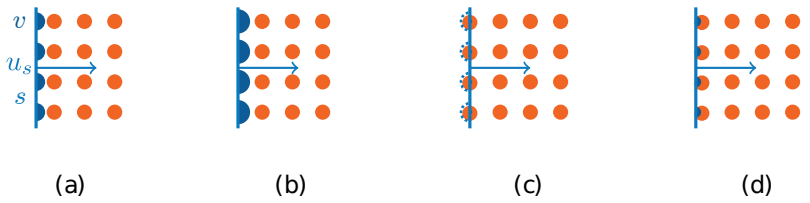

Figure 2: Sketch of the process of particles creation with vertices v and segments s at an inflow boundary [15]: a) the vertex masses grow due to the ingoing flux; b) their mass has reached the maximum threshold; c) new free particles are released and the vertex masses become negative (dashed line); d) the vertex masses start growing again.

with $\mathcal{N}_{sv}$ the set of segments s directly connected to v, N_{sv} its size, S_s the surface of segment s (or length in 2-D). At inflow boundaries, the mass flux (15) is positive and the mass of each vertex v increases until it reaches a higher threshold set to $+0.5m_{ref}$, with m_{ref} the mass of a free particle. Then, a free particle is created at the same location while m_{ref} is subtracted to m_v, so that m_v goes down to $-0.5m_{ref}$. Figure 2 illustrates that process. In this way the mass variation is smooth with respect to space and time. At outflow boundaries, the mass flux is negative and when a free particle crosses a segment to get out of the domain it is deleted and its mass is distributed onto the vertices directly linked to the segment, a weight $\beta_{a,v}$ being associated to each of these vertices. The weights are computed as in [15]:

- in 2-D, for v_0 and v_1 connected to s:

$$\begin{aligned} \beta_{a,v_0} &= \frac{\boldsymbol{p}_1 \cdot \boldsymbol{r}_{v_0 v_1}}{|\boldsymbol{r}_{v_0 v_1}|^2} \\ \beta_{a,v_1} &= \frac{\boldsymbol{p}_0 \cdot \boldsymbol{r}_{v_1 v_0}}{|\boldsymbol{r}_{v_0 v_1}|^2} = 1 - \beta_{a v_0} \end{aligned} \tag{16}$$

- in 3-D, for v_0, v_1 and v_2 connected to s:

$$\begin{aligned} \beta_{a,v_0} &= \frac{\frac{1}{2}[\boldsymbol{p}_2 \times \boldsymbol{r}_{v_2 v_1}] \cdot \boldsymbol{n}_s}{\frac{1}{2}[\boldsymbol{r}_{v_0 v_1} \times \boldsymbol{r}_{v_0 v_2}] \cdot \boldsymbol{n}_s} \\ \beta_{a,v_1} &= \frac{\frac{1}{2}[\boldsymbol{p}_0 \times \boldsymbol{r}_{v_0 v_2}] \cdot \boldsymbol{n}_s}{\frac{1}{2}[\boldsymbol{r}_{v_0 v_1} \times \boldsymbol{r}_{v_0 v_2}] \cdot \boldsymbol{n}_s} \\ \beta_{a,v_2} &= \frac{\frac{1}{2}[\boldsymbol{p}_1 \times \boldsymbol{r}_{v_1 v_0}] \cdot \boldsymbol{n}_s}{\frac{1}{2}[\boldsymbol{r}_{v_0 v_1} \times \boldsymbol{r}_{v_0 v_2}] \cdot \boldsymbol{n}_s} \end{aligned} \tag{17}$$

An illustration of the notations and of the fraction of segment area $\beta_{a,v}$ attributed to a vertex is provided on Figure 3. $\boldsymbol{p}_i$ is the projection of $\boldsymbol{r}_{av_i}$ on s:

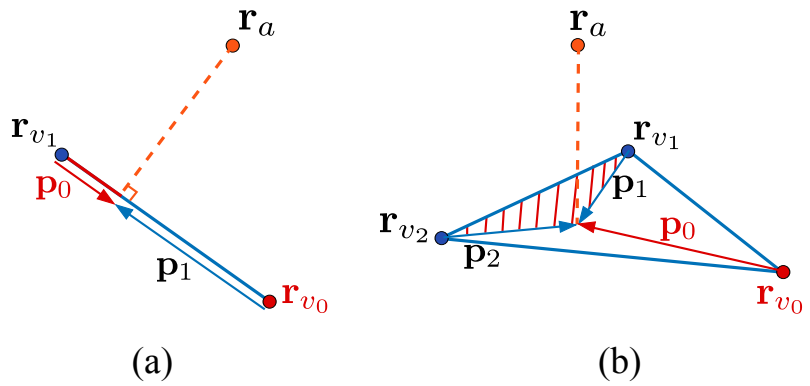

Figure 3: Open boundary technique based on the USAW boundary conditions: sketch of the notations for the computation of the fraction of segment area $\beta_{a,v}$ attributed to a vertex at the outlet [15]. (a) 2-D case; (b) 3-D case. The coefficient associated to the vertex v_0 is proportional to the red area so that the largest amount of mass goes to the closest vertex particle.

$\boldsymbol{p}_i = \boldsymbol{r}_{av_i} - (\boldsymbol{r}_{av_i} \cdot \boldsymbol{n}_s)\boldsymbol{n}_s$ (v_i being one of the vertices linked to s). In this way, the authors of [15] took care that the largest amount of mass is attributed to the closest vertex particle to the point where a fluid particle is destroyed. This aimed at making the mass displacement as small as possible.

The following mass evolution equation is thus solved at the end of each time-step $\forall v \in \mathcal{V}_{i/o}$:

$$m_v^{n+1} = m_v^n + \delta t \dot{m}_v^n + \delta m_v^n \tag{18}$$

with δm_v^n the mass variation due to particle creation/destruction and $\dot{m}_v^n$ the mass flux corresponding to the imposed velocity at the open boundary.

5.2. Imposition of the inflow/outflow boundary conditions

We consider two options for the prescription of inflow/outflow boundary conditions: either the velocity or the pressure is set. Generally, boundaries where the velocity is imposed are inflow boundaries whereas boundaries where the pressure is imposed are outflow boundaries, but this is not exhaustive. Indeed, the algorithm makes it possible for particles to leave the domain through a boundary with prescribed velocity, or to enter the domain through a boundary with prescribed pressure. In other words, inlet and outlet conditions can be handled by any open boundary at the same time. This is necessary in case of a prescribed recirculation close to an inlet. Then, at boundaries where the

velocity is prescribed a Dirichlet condition is also set on the temperature, and a homogeneous Neumann condition is set on the pressure. On the other hand, at boundaries where the pressure is prescribed a homogeneous Neumann condition is set on the velocity and temperature fields. Here the open boundary conditions on k and ϵ are not detailed: they are the same as for the temperature.

The imposition of these open boundary conditions is done in a similar way as for wall boundaries in [12, 33]: Dirichlet conditions are imposed at the vertex particles whereas the Neumann conditions are imposed through the segments by setting the boundary terms of the Laplacian operators. Compatible conditions are then deduced and imposed on the complementary entities (*i.e.* segments in case of a Dirichlet condition, vertex in case of a Neumann condition).

5.3. Boundaries with prescribed velocity

The Dirichlet condition on the Eulerian velocity $\boldsymbol{u}$ is imposed at the vertex particles in the correction step of the projection method (fifth line of (13)). The velocity gradient at the segments is then deduced through a linear interpolation involving the particles close to the boundary. The Dirichlet condition on T is imposed at the vertex particles and the normal temperature gradient is computed through a linear interpolation between the segments and the surrounding free particles. The homogeneous Neumann condition on the pressure is imposed through the pressure Laplacian in the pressure Poisson equation (fourth line of (13)). Moreover, the pressure of vertex particles belonging to an inlet is extrapolated from the surrounding fluid particles so that a homogeneous Neumann condition is imposed. This ensures that the pressure at the open boundary is compatible with the imposed velocity. Thus, the boundary conditions imposed during the time-scheme when the velocity is prescribed read:

$$\begin{cases} \boldsymbol{u}_v^{n+1} = \boldsymbol{u}_v^{pv} \\ T_v^{n+1} = T_v^{pv} \\ \left(\dfrac{\partial p}{\partial \boldsymbol{n}}\right)_s^{n+1} = 0 \end{cases} \tag{19}$$

The compatible conditions on the complementary entities read:

$$\begin{cases} \left(\dfrac{\partial \boldsymbol{u}}{\partial \boldsymbol{n}}\right)_s^{n+1} = \dfrac{\boldsymbol{u}_{as}}{\delta r_{as}} \cdot \boldsymbol{n}_s \\ \left(\dfrac{\partial T}{\partial \boldsymbol{n}}\right)_s^{n+1} = 0 \\ p_v^{n+1} = p_v^{pv} = \dfrac{1}{\alpha_v} \displaystyle\sum_{b \in \mathcal{F}} V_b p_b^n w_{vb} \end{cases} \tag{20}$$

where the superscript pv denotes the value of a field at an open boundary with prescribed velocity. In addition, δr_{as} is defined by

$$\delta r_{as} = \max(\boldsymbol{r}_{as} \cdot \boldsymbol{n}_s, \delta r) \tag{21}$$

and α_v is the Shepard filter:

$$\alpha_v = \sum_{b \in \mathcal{P}} V_b w_{vb} \tag{22}$$

The values of the fields at the segments of the boundary are then deduced from a mean of the directly linked vertex particles. The Neumann conditions in equations (19) and (20) are imposed in the boundary terms of the SPH Laplacian of T, p and $\boldsymbol{u}$ (second term in the right-hand side of (12)).

5.4. Boundaries with prescribed pressure

The Dirichlet condition on the pressure is imposed at the vertex particles. It can be either a fixed pressure value (like the hydrostatic pressure) or a radiative condition such as the one proposed by Orlanski [34], so as to let waves leave the domain:

$$\left(\frac{\partial p}{\partial t} + C \frac{\partial p}{\partial \boldsymbol{n}}\right)_{\partial \Omega_o} = 0 \tag{23}$$

with C a celerity usually taken as $\sqrt{gd}$, d being the initial elevation of the free-surface above the bed at the outlet which is given by the user. Then, the pressure condition reads:

$$\begin{cases} p_s^{pp} = p_s^n - \dfrac{C \delta t}{\alpha_s} \displaystyle\sum_{b \in \mathcal{F}} V_b \frac{p_b^n - p_s^n}{\delta r_{sb}} w_{sb} \\ p_v^{pp} = \dfrac{1}{N_{sv}} \displaystyle\sum_{s \in \mathcal{N}_{sv}} p_s^{pp} \end{cases} \tag{24}$$

where the superscript pp denotes the value of a field at an open boundary with prescribed pressure. The compatible Neumann condition imposed on the pressure is obtained through a linear interpolation of the surrounding free particles

pressure. On the other hand, the homogeneous Neumann condition on T and $\boldsymbol{u}$ is imposed at the segments in the boundary term of the Laplacian operator (12). A compatible Dirichlet condition is deduced through an interpolation on the surrounding free particles. Thus, the boundary conditions imposed during the time-scheme when the pressure is prescribed read:

$$\begin{cases} \left(\dfrac{\partial \boldsymbol{u}}{\partial \boldsymbol{n}}\right)_s^{n+1} = 0 \\ \left(\dfrac{\partial T}{\partial \boldsymbol{n}}\right)_s^{n+1} = 0 \\ p_v^{n+1} = p_v^{pp} \end{cases} \tag{25}$$

and for the complementary entities the compatible conditions read:

$$\begin{cases} \boldsymbol{u}_v^{n+1} = \dfrac{1}{\alpha_v} \displaystyle\sum_{b \in \mathcal{F}} V_b \boldsymbol{u}_b^{n+1} w_{vb} \\ T_v^{n+1} = \dfrac{1}{\alpha_v} \displaystyle\sum_{b \in \mathcal{F}} V_b T_b^{n+1} w_{vb} \\ \left(\dfrac{\partial p}{\partial \boldsymbol{n}}\right)_s^{n+1} = \dfrac{p_a^{n+1} - p_s^{pp}}{\delta r_{as}} \end{cases} \tag{26}$$

6. Solving the pressure Poisson equation

In the framework of the USAW boundary conditions, the pressure Poisson equation (second line of (13)) reads:

$$\begin{bmatrix} \dfrac{2}{\gamma_a} \displaystyle\sum_{b \in \mathcal{P}} V_b \frac{p_{ab}^{n+1}}{r_{ab}^2} \boldsymbol{r}_{ab} \cdot \boldsymbol{\nabla} w_{ab} \\ -\dfrac{2}{\gamma_a} \displaystyle\sum_{s \in \mathcal{S}} \boldsymbol{\nabla} p_s^{n+1} \cdot \boldsymbol{\nabla} \gamma_{as} \end{bmatrix} = \frac{\rho}{\delta t} D_a^{\gamma,-} \{\tilde{\boldsymbol{v}}_b^{n+1}\} \tag{27}$$

where the unknowns are the set of pressures p^{n+1} (recall that $p_{ab} = p_a - p_b$). Taking the boundary conditions described in sections 4 and 5 into account (equation (14) and 3rd lines of (19) and (26)) and keeping in the left-hand side only

the terms involving the unknown pressures, this equation becomes:

$$\begin{aligned}\frac{2}{\gamma_a}\left[\begin{array}{l}\displaystyle\sum_{b\in\mathcal{P}} V_b \frac{p_{ab}^{n+1}}{r_{ab}^2}\boldsymbol{r}_{ab}\cdot\boldsymbol{\nabla}w_{ab} \\ \displaystyle -\sum_{s\in\mathcal{S}_{pp}} \frac{p_a^{n+1}}{\delta r_{as}}|\boldsymbol{\nabla}\gamma_{as}|\end{array}\right] &= \frac{\rho}{\delta t} D_a^{\gamma,-}\{\tilde{\boldsymbol{v}}_b^{n+1}\} \\ &+\frac{2\rho}{\gamma_a}\sum_{s\in\mathcal{S}\setminus\mathcal{S}_{i/o}}\left(\frac{\tilde{\boldsymbol{v}}_s^{n+1}-\boldsymbol{v}_s^{wall}}{\delta t}\right)\cdot\boldsymbol{\nabla}\gamma_{as} \\ &-\frac{2}{\gamma_a}\sum_{s\in\mathcal{S}_{pp}}\frac{p_s^{pp}}{\delta r_{as}}|\boldsymbol{\nabla}\gamma_{as}|\end{aligned} \tag{28}$$

where $\mathcal{S}_{pp}$ is the set of open boundary segments with prescribed pressure. The lines of the matrix corresponding to inlet/outlet vertex particles are removed. Besides, the product of the columns corresponding to these particles with the unknown pressure vector is known (either through a Dirichlet condition or an approximation of a Neumann condition) and passed to the right-hand side. In the end the system to be solved does not involve the inlet/outlet particles anymore and they appear in the right-hand side:

$$\begin{aligned}\frac{2}{\gamma_a}\left[\begin{array}{l}\displaystyle\sum_{b\in\mathcal{P}\setminus\mathcal{V}_{i/o}} V_b \frac{p_{ab}^{n+1}}{r_{ab}^2}\boldsymbol{r}_{ab}\cdot\boldsymbol{\nabla}w_{ab} \\ \displaystyle +\sum_{b\in\mathcal{V}_{i/o}} V_b \frac{p_a^{n+1}}{r_{ab}^2}\boldsymbol{r}_{ab}\cdot\boldsymbol{\nabla}w_{ab} \\ \displaystyle -\sum_{s\in\mathcal{S}_{pp}} \frac{p_a^{n+1}}{\delta r_{as}}|\boldsymbol{\nabla}\gamma_{as}|\end{array}\right] &= \frac{\rho}{\delta t} D_a^{\gamma,-}\{\tilde{\boldsymbol{v}}_b^{n+1}\} \\ &+\frac{2\rho}{\gamma_a}\sum_{s\in\mathcal{S}\setminus\mathcal{S}_{i/o}}\left(\frac{\tilde{\boldsymbol{v}}_s^{n+1}-\boldsymbol{v}_s^{wall}}{\delta t}\right)\cdot\boldsymbol{\nabla}\gamma_{as} \\ &-\frac{2}{\gamma_a}\sum_{s\in\mathcal{S}_{pp}}\frac{p_s^{pp}}{\delta r_{as}}|\boldsymbol{\nabla}\gamma_{as}| \\ &+\frac{2}{\gamma_a}\sum_{b\in\mathcal{V}_{i/o}} V_b \frac{p_b^{i/o}}{r_{ab}^2}\boldsymbol{r}_{ab}\cdot\boldsymbol{\nabla}w_{ab}\end{aligned} \tag{29}$$

where $p_b^{i/o}$ denotes either p_b^{pv} or p_b^{pp}. This equation corresponds to a linear system:

$$\boldsymbol{A}\boldsymbol{p} = \boldsymbol{B} \tag{30}$$

where $\boldsymbol{p}$ is the unknown vector of all particles pressures p_a, $\boldsymbol{B}$ is the vector of right-hand side values at all particles and $\boldsymbol{A}$ is a sparse matrix corresponding to the discrete Laplacian operator. The Laplacian matrix is non-symmetric

because of the γ_a factor, of the term involving outlet segments and because V_b is not constant with the USAW boundary conditions: the volumes of the vertex particles are lower than that of the free particles. To solve system (30), the Bi-CGSTAB linear solver [35] is used.

7. 2-D validation

7.1. Schematic dam-break with an outflow condition

This case consists of a schematic dam-break on a flat bottom, which was cut so as to test the outlet formulation, and check that the fluid leaves the domain without reflections. The outlet boundary is the left-wall (at all times) in Figure 4, where the pressure is prescribed according to the Bernoulli equation: $p^{pp} = -\frac{1}{2}\rho v^{pp2}$. All the lengths are made dimensionless by the height of the fluid column at the initial time, d. The dimensionless width of the domain is equal to 1. The initial dimensionless interparticular space was taken equal to 6×10^{-3}. The viscosity of the fluid was set to a relatively large value, $10^{-2} m^2 s^{-1}$, because the ISPH model used here still suffers from particle leaks for free-surface flows with low viscosity (see [12]).

The dimensionless time is defined by:

$$t^+ = \frac{t}{\sqrt{gd}} \tag{31}$$

Figure 4 shows the velocity field shape at several dimensionless times. On the left boundary, some particles adhere to the wall due to the relatively high value of viscosity used for this case. The fluid correctly leaves the domain without visible reflections at the outlet. The free-surface shape of the same non-cut dam-break simulated with ISPH-USAW is provided and appears in black in the Figure. The agreement is good between the two simulations, which shows that the proposed formulation is reliable.

7.2. 2-D solitary wave

A case of propagation of a solitary wave on a slope is presented here, where the wave breaks before leaving the domain. It was chosen in order to qualitatively check that the proposed open boundary formulation makes it possible to generate waves and let them leave the computational domain without introducing too much perturbations in the flow. Figure 5 shows the geometry of

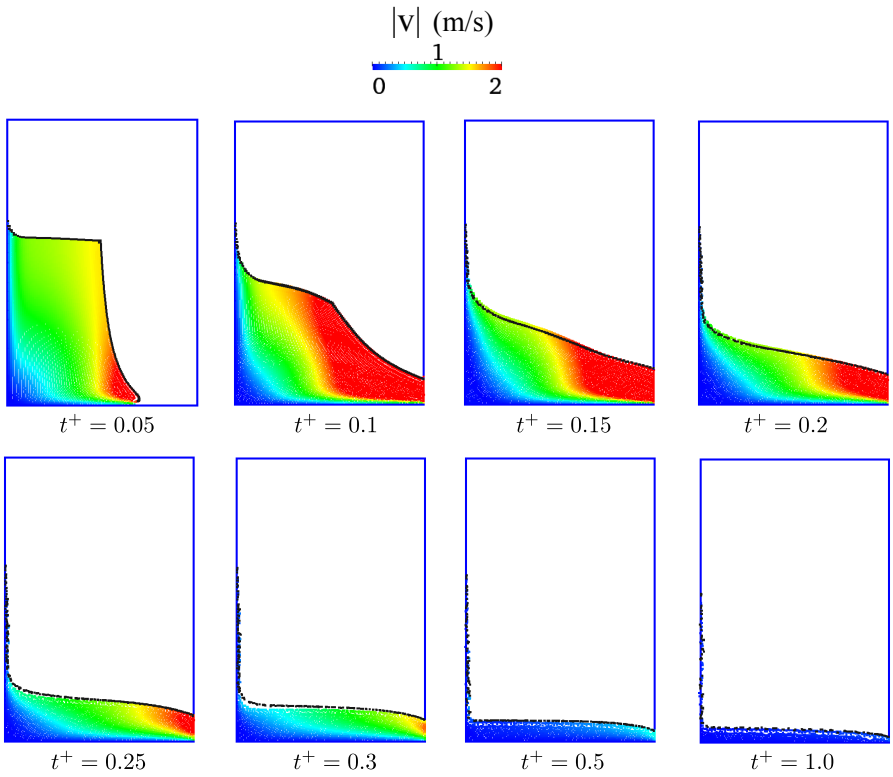

Figure 4: Dam-break with an outflow condition: velocity field shape obtained with the present ISPH-USAW model. Comparison with the free-surface shape of a non-cut dam-break (black dots).

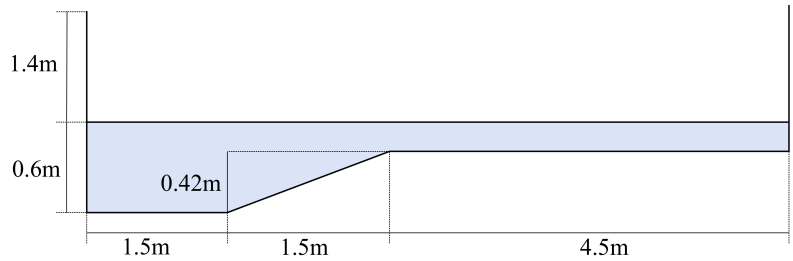

Figure 5: Sketch of the geometry of the case of propagation of a solitary wave on a slope.

the case. The incoming free-surface elevation is prescribed as a solitary wave (solution to the Korteveg-De Vries equation) [36]:

$$\eta(x,t) = A\text{sech}^2[k(x - Ct - x_0)] \tag{32}$$

where η is the free-surface elevation compared to a reference water level d, A is the wave amplitude, taken as $A = \frac{d}{2}$, $k = \sqrt{\frac{3A}{4d^3}}$ is the wave number and $C = \sqrt{g(A+d)}$ is the wave celerity. x_0 is the initial position of the wave, equal to $x_0 = x_{inlet} - \frac{4}{k}$ here. At the inlet (left boundary in Figure 5), the time-dependent water height d_t is used to impose the following velocity profile:

$$\begin{cases} d_t(t) = d + \eta(x_{inlet}, t) \\ u_x(z,t) = C\dfrac{\eta(x_{inlet},t)}{d(t)} \\ u_z(z,t) = \dfrac{z}{d_t(t)}\dfrac{\partial \eta}{\partial t}(x_{inlet},t) \end{cases} \tag{33}$$

with x_{inlet} the horizontal coordinate of the inlet. At the outlet (right boundary in Figure 5), the pressure is imposed through the Orlanski radiative boundary condition (24) with a celerity of $\sqrt{gd}$.

Figure 6 shows the propagation of the solitary wave on the slope with a dynamic molecular viscosity of $10^{-6}m^2s^{-1}$ (no turbulence model was used in the simulation). The dimensionless time t^+ is defined as in the previous section, through (31). The colours correspond to the pressure field obtained with ISPH-USAW. This simulation was run with 30315 particles ($\delta r = 0.01m$). The wave correctly enters the domain and leaves it after breaking, apparently without reflections, although there was no attempt at quantifying the amount of reflection in the domain.

This shows that the proposed open boundary formulation makes it possible

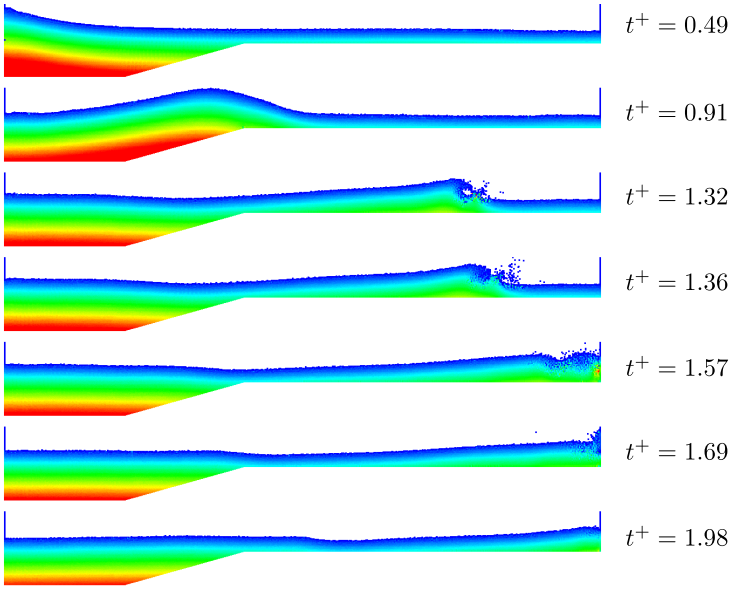

Figure 6: Propagation of a solitary wave on a slope with $\nu = 10^{-6} m^2 s^{-1}$: pressure field obtained with ISPH-USAW ranging from $0Pa$ to $5837Pa$ (blue to red).

to generate waves and let them leave the computational domain quite smoothly, even when the free-surface shape is complex due to wave breaking.

7.3. Creager Weir

A Creager weir is a spillway with a geometry such that for a given upstream head (called the dimensioning head H_d), the pressure on the weir is equal to the atmospheric pressure. The weir has a width L, which will not be considered here, as we are in a 2D simulation. The geometry is described on Figure 7.

The upstream face, between points M_1 and M_2, is defined by three arcs of circles having centres with coordinates x_i and z_i and radii R_i. Their values and the arc boundaries are given in [37]. The downstream face is given by:

$$\frac{z}{H_d} = -\frac{1}{2}\left(\frac{x}{H_d}\right)^{1.85} \tag{34}$$

The hydraulic head is defined with:

$$H = \frac{1}{2g}U^2 + d + \frac{P_{atm}}{\rho g} \tag{35}$$

where U is the velocity, d the water depth and P_{atm} the atmospheric pressure.

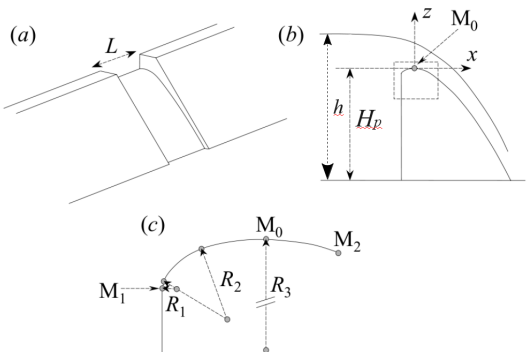

Figure 7: Creager weir geometry, from [37] after US Army Corps of Engineers (1990). Overall view (a), vertical profile in the indented area (b) and zooming in on the area surrounded by a dashed line (c).

Dimensional analysis gives the flow rate per meter q as a function of g, H, a function $C_q\left(\frac{H}{H_d}, \frac{H}{H_p}\right)$ and H_p the weir height, see Figure 7:

$$q = \sqrt{2gH^3} C_q \left(\frac{H}{H_d}, \frac{H}{H_p}\right) \tag{36}$$

The function C_q is also called the discharged coefficient, it is determined by experiments [38]:

$$C_q = C_p \left(\frac{H}{H_d}\right)^{0.12} \tag{37}$$

From experiments C_p can be set as $C_p \approx 0.485$. Here, the value of the dimensional head is chosen as $H_d = 0.3m$, and a weir height $H_p = 0.4m$. We choose to simulate two steady cases of imposed upstream head: $H/H_d = 0.5$ and $H/H_d = 1.33$. With the relations (36) and (37) and knowing that $q = hU$, the water depth d and the bulk velocity U at inlet can be deduced. The inlet condition is imposed at a distance $4H_p$ before the weir. At the beginning of the simulation, the fluid is at rest and the pressure is set as hydrostatic: $p(z) = \rho g(d - z)$ (z is the vertical elevation above the bed). For this case the $k-\epsilon$ turbulence closure was used. At the inlet, a logarithmic horizontal velocity profile is imposed, with the corresponding k and ϵ profiles [24]:

$$\begin{cases} u(z) = u_* \left(\frac{1}{\kappa} \ln \frac{z u_*}{\nu} + C_r\right) \\ k(z) = \frac{{u_*}^2}{\sqrt{C_\mu}} \left(1 - \frac{z}{d}\right) \\ \epsilon(z) = \frac{{u_*}^3}{\kappa z} \left(1 - \frac{z}{d}\right) \end{cases} \tag{38}$$

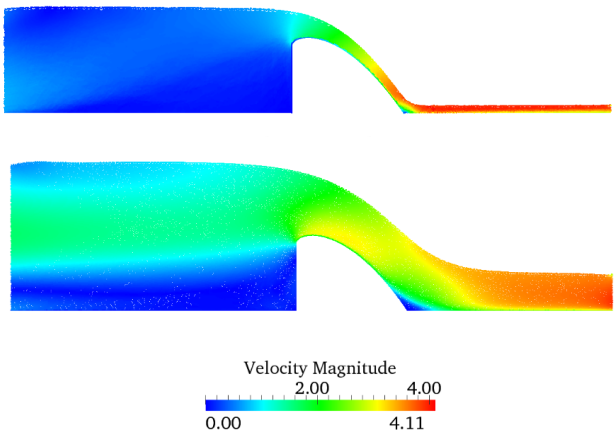

Figure 8: Creager weir case. Velocity field for a flow on a Creager weir for $H/H_d = 0.5$ (top) and $H/H_d = 1.33$ (bottom) with ISPH-USAW (flow from left to right).

Here, u_* is the shear velocity upstream of the weir, $\nu = 10^{-6} m^2/s$ the kinematic viscosity of water, $\rho = 1000 kg/m^3$ the reference density and $C_r = 5.2$ is a constant. The mean (depth-averaged) velocity U is given by:

$$U = u_* \left[\frac{1}{\kappa} \left(\ln \frac{u_* d}{\nu} - 1 \right) + C_r \right] \tag{39}$$

Knowing U and d, the shear velocity is iteratively computed. The imposed water depth, mean velocity and shear velocity are summarised in Table 2. At the outlet, we want to let the flow go out. To be correct, a hydrostatic pressure should be imposed. However, as the water depth is not known in advance, the pressure is imposed at zero.

Figure 8 shows the velocity field obtained at steady-state for the two configurations with ISPH-USAW, using $\delta r = 0.0125 H_p$. The free-surface position and pressure along the weir obtained with ISPH-USAW are compared to experimental results [39] for each configuration. The results are shown in Figure 9. The free-surface position obtained with ISPH-USAW shows quite good agreement with the experiment data, and the pressure along the weir shows reasonable agreement. The results obtained for the configuration with the lower head upstream match the experiments better than with the higher head. With the higher head, a pressure peak is observed in front of the weir in the numerical results. This is probably due to an issue with the convergence of the pressure

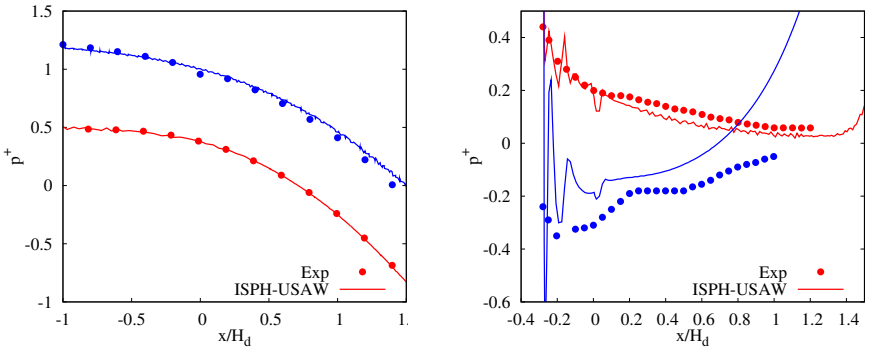

Figure 9: Creager weir case. Free surface (left) and pressure (right) on weir for $H/H_d = 0.5$ (red) and $H/H_d = 1.33$ (blue). Both are mean values over $3s$ once the flow has reached a steady state. The dimensionless pressure is $p^+ = p/\rho g d$. The dots stand for experimental data [39] and the lines stand for ISPH-USAW.

solver (in our case Bi-CGSTAB), but the cause of it has not been identified. A similar behaviour was observed on a case of a schematic dam-break over an obstacle, both with an SPH formulation and with a two-phase Finite Volume formulation using the Volume of Fluid technique for the free-surface (see [12]).

8. 3-D cases

8.1. Laminar Poiseuille flow in a circular pipe with inflow/outflow boundaries

This case consists of a steady laminar flow through a 3-D pipe with a circular cross-section. Inflow and outflow boundaries are imposed at the extremities of the pipe. All lengths are made dimensionless by L, the radius of the cross-section. The dimensionless length of the pipe is equal to 4. The reference velocity of the flow U is the maximum velocity in the pipe, set to $1ms^{-1}$ by imposing the theoretical dimensionless velocity at the inlet:

$$\boldsymbol{v}^+ = \left[1 - (y^+ - y_0^+)^2 + (z^+ - z_0^+)^2\right] \boldsymbol{e}_x \tag{40}$$

where $(y_0^+, z_0^+) = (0, 0)$ are the dimensionless transverse and vertical coordinates of the cross-section centre. At the outlet, a zero-pressure is imposed. The Reynolds number is set to 10. The dimensionless time is defined by $t^+ = \frac{tU}{L}$. The simulation is run until $t^+ = 25$, which corresponds to about 1.4×10^5 iterations with an initial dimensionless interparticular space $\delta r^+ = 0.04$. A steady-state is then achieved. Figure 10 shows the shape of the velocity field in the pipe at $t^+ = 25$.

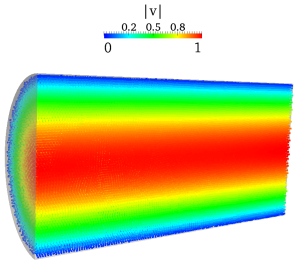

Figure 10: Steady laminar flow in a 3-D circular pipe with inflow/outflow conditions. Shape of the velocity profile obtained with ISPH-USAW using $\delta r^+ = 0.04$ at $t^+ = 25$ (flow from right to left).

Figure 11 shows velocity and pressure profiles in the pipe at $t^+ = 25$. On the left, the horizontal dimensionless velocity v_x^+ obtained with ISPH-USAW is plotted as a function of z^+ along the vertical profile at the centre of the channel ($x^+ = 2$, $y^+ = 0$). Note that the same results were obtained on a vertical profile in $y^+ = 0$ but at $x^+ = 3.9$ instead of $x^+ = 2$. Good agreement with the theoretical parabolic profile (40) is obtained. The dimensionless pressure is defined by:

$$p^+ = \frac{p}{\rho U^2/2} \tag{41}$$

On the right of Figure 11, the dimensionless pressure p^+ obtained with ISPH-USAW is plotted as a function of x^+ along the horizontal profile at the centre of the channel. The agreement with the theoretical linear pressure distribution along the channel is good, the latter being given by:

$$p^+ = \frac{8}{Re}\left(4 - x^+\right) \tag{42}$$

where $Re = \frac{UL}{\nu}$. A small discrepancy close to the inflow boundary appears, where a homogeneous Neumann condition is imposed on the pressure. Nevertheless, the quality of the results shows that the 3-D ISPH-USAW model performs well with inflow/outflow conditions for this Reynolds number.

It should be noted that trying to increase the Reynolds number leads to numerical instability. With a Reynolds of 100 the results are as good as with a Reynolds of 10, but with a Reynolds of 1000 a blow-up of the simulation occurred after some time. This issue points out the fact that further work is necessary for high-Reynolds simulations in 3D. It is worth mentioning that increasing the Reynolds number in SPH can be challenging, as pointed out e.g. in [40].

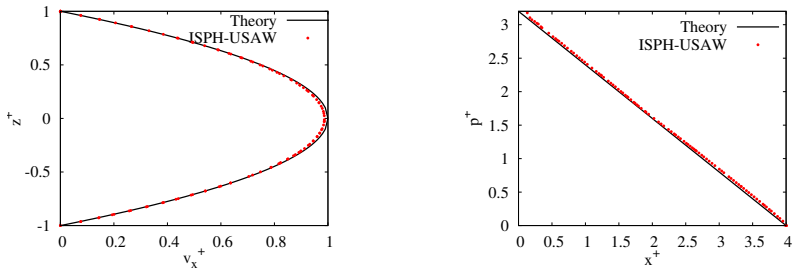

Figure 11: Steady laminar flow in a 3-D circular pipe with inflow/outflow conditions. Dimensionless velocity profile along the vertical line at the centre of the channel (left) and dimensionless pressure profile along the horizontal line at the centre of the channel (right). Comparison of the results obtained with ISPH-USAW using $\delta r^+ = 0.04$ with the theoretical velocity and pressure profiles.

Finally, Figure 12 shows the evolution of the total mass of particles in the domain. The total mass tends to a constant which shows that a steady state is reached, however some mass peaks are observed with a periodic pattern. The time between two peaks is that spent by a particle to go through half of the pipe's length and the mass fluctuations in steady state are in the range of one layer of particles on the cross-section of the pipe.

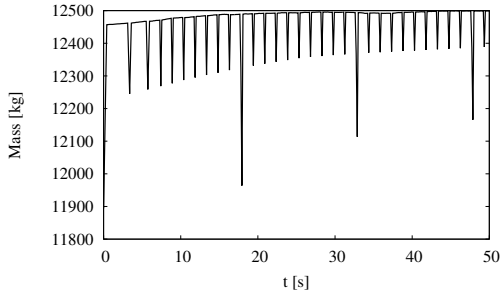

Figure 12: Laminar flow in a 3-D circular pipe with inflow/outflow conditions. Evolution of the total mass of particles in the computational domain using $\delta r^+ = 0.04$.

8.2. Preliminary application case: 3-D non-isothermal connected pipes

This case is a preliminary application case in 3-D that consists of two connected circular pipes at different temperatures. The geometry is described in the Figure 13. The reference length L is the diameter of the larger pipe. At the initial time, fluid with temperature T_h is placed in a horizontal pipe with zero velocity and pressure and fluid with temperature T_c ($T_c < T_h$) is placed in a

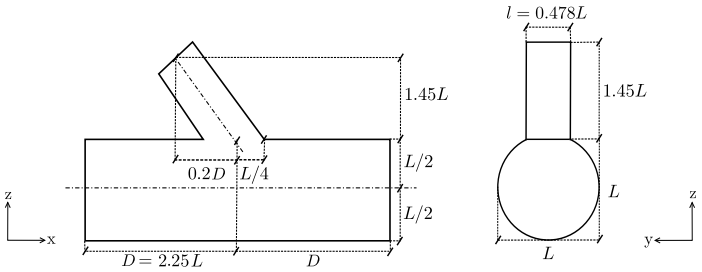

Figure 13: Laminar flow in two connected pipes at different temperatures. Sketch of the geometry.

smaller inclined pipe connected to the first one with zero velocity and pressure. As time goes by, fluid with temperature T_h is injected through the left extremity of the horizontal pipe and fluid with temperature T_c is injected at the highest extremity of the inclined pipe. The velocity is imposed at these inflow boundaries. In the horizontal pipe, it is imposed through a circular laminar Poiseuille profile:

$$\boldsymbol{v} = U \left[1 - \frac{\|\boldsymbol{x} - \boldsymbol{x_0}\|^2}{(L/2)^2} \right] \boldsymbol{n}_0 \tag{43}$$

where $\boldsymbol{x_0}$ is the position of the centre of the big pipe cross-section at the inlet, and $\boldsymbol{n}_0 = \boldsymbol{e}_x$ is the unit normal vector to that cross-section. U is the reference velocity of the flow and was set to $0.5ms^{-1}$. The Reynolds number based on U and L was set to 10. On the other hand, in the inclined pipe the inlet velocity is imposed through

$$\boldsymbol{v} = \frac{U}{2} \left[1 - \frac{\|\boldsymbol{x} - \boldsymbol{x_1}\|^2}{(l/2)^2} \right] \boldsymbol{n}_1 \tag{44}$$

where $\boldsymbol{x_1}$ is the position of the centre of the small pipe cross-section at this inlet, and $\boldsymbol{n}_1 = \left(-\frac{1}{\sqrt{3}}, 0, -\frac{2}{\sqrt{3}} \right)$ is the unit normal vector to that cross-section. An outflow boundary condition is imposed at the right extremity of the horizontal pipe: the pressure is imposed to zero and a homogeneous Neumann condition is imposed on the temperature. A homogeneous Neumann condition is also imposed on the temperature at solid walls. The Grashoff number $\frac{\beta g \Delta T L^3}{\nu^2}$ was set to 0.162, and the molecular Prandtl number $\frac{\nu}{K}$ to 69. Figure 14 shows the shape of the temperature field at several instants during the simulation.

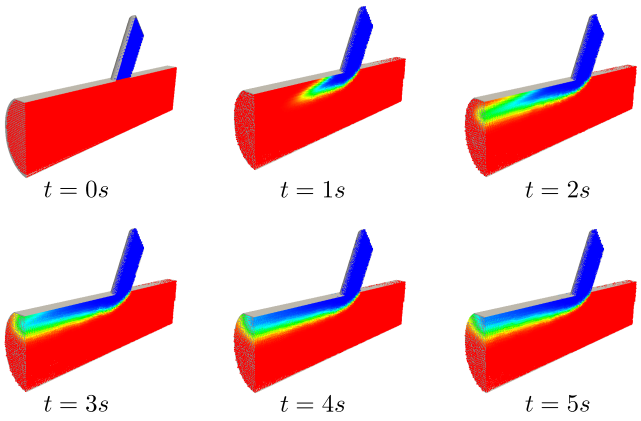

Figure 14: Laminar flow in two connected pipes at different temperatures. Shape of the temperature field at several times.

9. Conclusion

In this work a new formulation for inflow/outflow conditions in an ISPH model was proposed. The boundary conditions rely on the unified semi-analytical technique, which makes it possible to accurately prescribe Neumann or Dirichlet boundary conditions on the fields. The fluid enters and leaves the domain through the mass variation of boundary particles and their creation/destruction.

Validation was performed on several 2-D cases presenting open boundaries: a cut dam-break, a case of propagation of a solitary wave and a Creager weir, the latter involving the $k - \epsilon$ turbulence closure. The results show that the inflow/outflow conditions are able to let the fluid enter or leave the domain as prescribed, with few visible reflections in the domain. To go further, the outflow boundary conditions could be improved: the outflow boundary condition used for the wave case is quite a simple formulation for a radiative outlet and could be made more complex and more effective. On the other hand, a zero pressure was imposed at the outflow boundary on the cut dam-break, but a better condition could probably be designed. The conditions proposed in the literature for Eulerian methods could probably be applied in the framework of SPH, but this has not been tested extensively yet. To our knowledge, the question of free outlet conditions is quite problematic in the framework of Eulerian methods as well.

Finally, one case of validation in 3-D is also presented, as well as prelimi-

nary results on a simple application case involving temperature effects in 3-D. Further work in 3-D is necessary since instabilities were observed when simulating 3-D flows with high Reynolds numbers using the present formulation for inflow/outflow boundaries.

Acknowledgements

This work was partly funded by the French Research Agency (CIFRE grant agreement # 2011-0264).

References

[1] J. J. Monaghan, "Smoothed particle hydrodynamics," *Reports on Progress in Physics*, vol. 68, pp. 1703–1759, 2005.

[2] J. J. Monaghan and J. Kajtar, "SPH particle boundary forces for arbitrary boundaries," *Computer Physics Communications*, vol. 180, no. 10, pp. 1811–1820, 2009.

[3] S. Shao and E. Y. M. Lo, "Incompressible SPH method for simulating Newtonian and non-Newtonian flows with a free-surface," *Advanced Water Ressources*, vol. 26, pp. 787–800, 2003.

[4] R. Issa, "Numerical assessment of the smoothed particle hydrodynamics gridless method for incompressible flows and its extension to turbulent flows," Ph.D. dissertation, University of Manchester, Manchester, 2004.

[5] E.-S. Lee, C. Moulinec, R. Xu, D. Violeau, D. Laurence, and P. K. Stansby, "Comparisons of weakly compressible and truly incompressible algorithms for the SPH mesh free particle method," *Journal of Computational Physics*, vol. 227, pp. 8417–8436, 2008.

[6] G. Oger, C. Leroy, E. Jacquin, D. Le Touzé, and B. Alessandrini, "Specific pre/post treatments for 3-D SPH applications through massive HPC simulations," in *Proc. 4th international SPHERIC workshop*, 2009, pp. 27–29.

[7] S. Kulasegaram, J. Bonet, R. W. Lewis, and M. Profit, "A variational formulation based contact algorithm for rigid boundaries in two-dimensional SPH applications," *Computational Mechanics*, vol. 33, pp. 316–325, 2004.

[8] J. Feldman and J. Bonet, "Dynamic refinement and boundary contact forces in SPH with applications in fluid flow problems," *International Journal for Numerical Methods in Engineering*, vol. 72, pp. 295–324, 2007.

[9] M. Ferrand, D. Laurence, B. D. Rogers, and D. Violeau, "Improved time scheme integration approach for dealing with semi analytical boundary conditions in SPARTACUS2D," in *Proc. 5th international SPHERIC workshop*, 2010.

[10] M. Ferrand, D. R. Laurence, B. D. Rogers, D. Violeau, and C. Kassiotis, "Unified semi-analytical wall boundary conditions for inviscid, laminar or turbulent flows in the meshless SPH method," *International Journal for Numerical Methods in Fluids*, vol. 71, pp. 446–472, 2013.

[11] A. Mayrhofer, B. D. Rogers, D. Violeau, and M. Ferrand, "Investigation of wall bounded flows using SPH and the unified semi-analytical wall boundary conditions," *Computer Physics Communications*, vol. 184, no. 11, pp. 2515–2527, 2013.

[12] A. Leroy, D. Violeau, M. Ferrand, and C. Kassiotis, "Unified semi-analytical wall boundary conditions applied to 2-D incompressible SPH," *Journal of Computational Physics*, vol. 261, pp. 106–129, Mar. 2014.

[13] D. Violeau, A. Leroy, and A. Mayrhofer, "Exact computation of SPH wall renormalising integrals in 3-D," in *Proc. 9th international SPHERIC workshop*, 2014.

[14] R. Vacondio, B. D. Rogers, P. K. Stansby, and P. Mignosa, "SPH modeling of shallow flow with open boundaries for practical flood simulation," *Journal of Hydraulic Engineering*, vol. 138, no. 6, pp. 530–541, 2011.

[15] C. Kassiotis, D. Violeau, and M. Ferrand, "Semi-analytical conditions for open boundaries in smoothed particle hydrodynamics," in *Proc. 8th international SPHERIC workshop*, 2013.

[16] M. Hirschler, P. Kunz, M. Huber, F. Hahn, and U. Nieken, "Open boundary conditions for ISPH and their application to micro-flow," *Journal*

of Computational Physics, vol. 307, pp. 614–633, Feb. 2016. [Online]. Available: http://linkinghub.elsevier.com/retrieve/pii/S0021999115008438

[17] O. Mahmood, D. Violeau, C. Kassiotis, B. D. Rogers, and M. Ferrand, "Absorbing inlet/outlet boundary conditions for 2D SPH turbulent free-surface flows," in *Proc. 7th international SPHERIC workshop*, 2012, pp. 296–302.

[18] R. Xu, P. K. Stansby, and D. Laurence, "Accuracy and stability in incompressible SPH (ISPH) based on the projection method and a new approach," *Journal of Computational Physics*, vol. 228, no. 18, pp. 6703–6725, 2009.

[19] P. Nair and G. Tomar, "An improved free surface modeling for incompressible SPH," *Computers & Fluids*, vol. 102, pp. 304–314, Oct. 2014. [Online]. Available: http://linkinghub.elsevier.com/retrieve/pii/S0045793014002850

[20] M. Yildiz, R. A. Rook, and A. Suleman, "SPH with the multiple boundary tangent method," *International Journal for Numerical Methods in Engineering*, vol. 77, pp. 1416–1438, 2009.

[21] D. Violeau, S. Piccon, and J.-P. Chabard, *Two attempts of Turbulence Modelling in Smoothed Particle Hydrodynamics, Advances in Fluid Modelling and Turbulence Measurements.* World Scientific, 2002.

[22] D. Violeau, "One and two-equations turbulent closures for Smoothed Particle Hydrodynamics," in *6th Int. Conf. Hydroinformatics*, Singapore, 2004, pp. 87–94.

[23] J.-M. Hervouet, *Hydrodynamics of Free Surface Flows: Modelling with the Finite Element Method.* John Wiley, 2007.

[24] B. E. Launder and D. B. Spalding, *Mathematical models of turbulence.* London: Academic Press, 1972.

[25] W. Rodi, "Turbulence models and their applications in hydraulics," in *IAHR monograph*, Brookfield, Rotterdam, 2000.

[26] V. Guimet and D. Laurence, "A linearised turbulent production in the k-ϵ model for engineering applications," in *Proc. Vth International Symposium on Engineering Turbulence Modelling and Measurements*, 2002, pp. 157–166, majorqua (Spain).

[27] H. Wendland, "Piecewise polynomial, positive definite and compactly supported radial functions of minimal degree," *Advances in Computational Mathematics*, vol. 4, pp. 389–396, 1995.

[28] A. Mayrhofer, M. Ferrand, C. Kassiotis, D. Violeau, and F.-X. Morel, "Unified semi-analytical wall boundary conditions in SPH: analytical extension to 3-d," *Numerical Algorithms*, 2014.

[29] S. J. Cummins and M. Rudman, "An SPH projection method," *Journal of Computational Physics*, vol. 152, no. 2, pp. 584–607, 1999.

[30] A. J. Chorin, "On convergence of discrete approximations to the Navier-Stokes equations," *Mathematics of Computation*, vol. 23, pp. 341–353, 1969.

[31] S. Lind, R. Xu, P. K. Stansby, and B. D. Rogers, "Incompressible smoothed particle hydrodynamics for free-surface flows: A generalised diffusion-based algorithm for stability and validations for impulsive flows and propagating waves," *Journal of Computational Physics*, vol. 231, no. 4, pp. 1499–1523, 2012.

[32] D. Violeau and A. Leroy, "Optimal time-step for incompressible SPH," *Journal of Computational Physics*, 2015.

[33] A. Leroy, D. Violeau, M. Ferrand, and A. Joly, "Buoyancy modelling with incompressible sph for laminar and turbulent flows," *Int. J. Numer. Meth. Fluids*, 2015.

[34] I. Orlanski, "A simple boundary condition for unbounded hyperbolic flows," *Journal of Computational Physics*, vol. 21, pp. 251–269, 1976.

[35] H. A. V. D. Vorst, "Bi-CGSTAB: a fast and smoothly converging variant of Bi-CG for the solution of nonsymmetric linear systems," *Journal on Scientific and Statistical Computing*, vol. 13, no. 2, pp. 631–644, 1992.

[36] R. G. Dean and R. A. Dalrymple, *Water wave mechanics for engineers and scientists, volume 2 of Advanced Series on Ocean Engineering.* World Scientific, Singapore, 1991.

[37] D. Violeau, *Fluid Mechanics and the SPH method.* Oxford University Press, 2012.

[38] V. T. Chow, *Open-Channel Hydraulics.* New-York, USA: McGraw-Hill, 1959.

[39] USBR, "Design of small dams."

[40] S. Adami, X. Y. Hu, and N. A. Adams, "A transport-velocity formulation for smoothed particle hydrodynamics," *Journal of Computational Physics*, 2013, accepted for publication.

Table 1: Values of the $k-\epsilon$ model constants [24]

κ	C_μ	C_{ϵ_1}	C_{ϵ_2}	σ_k	σ_ϵ
0.41	0.09	1.44	1.92	1.0	1.3

Table 2: Parameters for the Creager weir numerical simulations

H/H_d	0.5	1.33
$H(m)$	0.15	0.399
$q(m^3/s/m)$	0.115	0.560
$d(m)$	0.547	0.78
$U(m/s)$	0.21	0.72
$Fr = U/\sqrt{gd}$	0.09	0.26
$u_*(m/s)$	0.0089	0.0266
Domain length after the weir (m)	1	2.6